

FIRST SPECTROSCOPIC IDENTIFICATION OF MASSIVE YOUNG STELLAR OBJECTS IN THE GALACTIC CENTER

DEOKKEUN AN¹, SOLANGE V. RAMÍREZ¹, KRIS SELLGREN², RICHARD G. ARENDT^{3,4}, A. C. ADWIN BOOGERT¹,
MATHIAS SCHULTHEIS^{5,6}, SUSAN R. STOLOGY⁷, ANGELA S. COTERA⁸,
THOMAS P. ROBITAILLE^{9,10}, AND HOWARD A. SMITH⁹

Revised after referee report

ABSTRACT

We report the detection of several molecular gas-phase and ice absorption features in three photometrically-selected young stellar object (YSO) candidates in the central 280 pc of the Milky Way. Our spectra, obtained with the Infrared Spectrograph (IRS) onboard the *Spitzer Space Telescope*, reveal gas-phase absorption from CO₂ (15.0 μm), C₂H₂ (13.7 μm) and HCN (14.0 μm). We attribute this absorption to warm, dense gas in massive YSOs. We also detect strong and broad 15 μm CO₂ ice absorption features, with a remarkable double-peaked structure. The prominent long-wavelength peak is due to CH₃OH-rich ice grains, and is similar to those found in other known massive YSOs. Our IRS observations demonstrate the youth of these objects, and provide the first spectroscopic identification of massive YSOs in the Galactic Center.

Subject headings: infrared: ISM — ISM: molecules — stars: formation

1. INTRODUCTION

The Central Molecular Zone (CMZ) is the innermost ~ 200 pc region of the Milky Way Galaxy. It is a giant molecular cloud complex delineated by a gradient in the CO column density and temperature. The CMZ contains ~ 10% of the Galaxy's molecular gas, and produces 5%–10% of its infrared and Lyman continuum luminosities (see a review by Morris & Serabyn 1996, and references therein).

Evidence is mounting that conditions for star formation in the CMZ are significantly different from those in the Galactic disk. The gas pressure and temperature are higher in the CMZ than in the average disk, conditions that favor a larger Jeans mass for star formation and an initial mass function biased towards more massive stars. Furthermore, the presence of strong magnetic fields, tidal shear, and turbulence challenges the standard paradigm of slow gravitational collapse of molecular cloud cores.

The CMZ provides several signposts of *in situ* star formation, such as H₂O masers, (ultra-)compact H II regions, young OB stars, and young supernova remnants. However, young stellar objects (YSOs or protostars), which are the direct tracers of current star formation, have so far eluded detection in the CMZ. They have been inferred to be present based on infrared photometry (e.g., Felli et al. 2002; Schuller et al. 2006;

Yusef-Zadeh et al. 2009), but spectroscopic observations are required to confirm their status as a YSO. This is because evolved stars can look like YSOs in broad-band photometry, if they are heavily dust attenuated (e.g., Schultheis et al. 2003), a problem towards the Galactic Center (GC), where $A_V \approx 30$.

In this *Letter*, we present spectroscopic follow-up observations of YSO candidates in the CMZ, using the Infrared Spectrograph (IRS; Houck et al. 2004) onboard the *Spitzer Space Telescope* (Werner et al. 2004). Massive YSO candidates were photometrically selected from the point source catalog (Ramírez et al. 2008), which was extracted from images of the CMZ (Stolovy et al. 2006) made using the Infrared Array Camera (IRAC; Fazio et al. 2004). This high sensitivity and high spatial resolution image has led to a better identification of YSO candidates and their follow-up spectroscopic observations.

2. PHOTOMETRIC SAMPLE SELECTION

The IRAC point source catalog (Ramírez et al. 2008) contains photometry for more than a million point sources in the entire CMZ (2° × 1.4° or 280 × 200 pc) in four channels (3.6 μm, 4.5 μm, 5.8 μm, and 8.0 μm). Initially, we selected point sources with [3.6]–[8.0] ≥ 2.0, corresponding to YSOs with $M_* \gtrsim 2.5M_\odot$ (Whitney et al. 2003, 2004). We further confined the sample to those within $|b| < 15'$, resulting in 1207 objects. When we had photometric measurements in at least 5 bandpasses from IRAC, 2MASS (JHK_s ; Skrutskie et al. 2006), and/or ISOGAL (7 μm and 15 μm; Omont et al. 2003), we selected YSO candidates by comparing the observed spectral energy distribution (SED) with YSO models (Robitaille et al. 2006) using a SED fitting tool by Robitaille et al. (2007). Otherwise, we applied additional color constraints from Whitney et al. (2004, [3.6]–[4.5] ≥ 0.5, [4.5]–[5.8] ≥ 0.5, and [5.8]–[8.0] ≥ 1.0) to identify YSO candidates. SED fitting and color selection narrowed down our sample to about 200 objects.

Then, we carefully inspected IRAC three-color images to select objects that are distinct within the IRS slit entrances against the crowded stellar field and bright local background. Finally, a literature search was carried out for the selected objects, and one Wolf-Rayet star and four OH/IR stars were dis-

¹ Infrared Processing and Analysis Center, California Institute of Technology, Mail Stop 100-22, Pasadena, CA 91125; deokkeun@ipac.caltech.edu, solange@ipac.caltech.edu.

² Department of Astronomy, Ohio State University, 140 West 18th Avenue, Columbus, OH 43210; sellgren@astronomy.ohio-state.edu.

³ CRESST/UMBC/GSFC, Code 665, NASA/Goddard Space Flight Center, 8800 Greenbelt Road, Greenbelt, MD 20771.

⁴ Science Systems and Applications, Inc.

⁵ Observatoire de Besançon, 41bis, avenue de l'Observatoire, F-25000 Besançon, France.

⁶ Institut d'Astrophysique de Paris, CNRS, 98bis Bd Arago, F-75014 Paris, France.

⁷ Spitzer Science Center, California Institute of Technology, Mail Code 220-6, 1200 East California Boulevard, Pasadena, CA 91125.

⁸ SETI Institute, 515 North Whisman Road, Mountain View, CA 94043.

⁹ Harvard-Smithsonian Center for Astrophysics, 60 Garden Street, Cambridge, MA 02138.

¹⁰ Spitzer Postdoctoral Fellow.

carded. Our final sample is composed of 107 objects, among which 25 were previously known YSO candidates from ISO-GAL (Felli et al. 2002).

3. IRS OBSERVATIONS AND DATA REDUCTION

We obtained spectroscopic data for 107 YSO candidates using the four IRS modules in May and October 2008. We observed each target in IRS staring mode with 4 exposures per source (2 cycles). Exposure times were 6 sec–120 sec in SH (short-high; short wavelength, high resolution), 6 sec–60 sec in LH (long-high), 6 sec–14 sec in SL (short-low), and 6 sec in LL (long low) modules, depending on the source’s brightness, to achieve a signal-to-noise ratio (S/N) of at least 50 in SH and SL, and a minimum S/N of 10 in LH and LL. We reduced the IRS spectra from the basic calibrated data (BCD) products version S17.2.0 and S18.1.0, using the SSC software packages IRSCLEAN (to correct for bad pixel values) and SPICE (to extract spectra).

Because the GC exhibits strong, spatially variable background, we observed multiple off-source measurements (one cycle, 1×1 mapping mode) to derive backgrounds near each of our YSO candidates in the four IRS modules. The on-source and the off-source observations were taken consecutively to minimize zodiacal light and instrumental variations. For the high resolution observations, we observed and extracted four background positions ($\sim \pm 1'$ offsets in either R.A. or Decl.). For the low resolution observations, we took spectra from two background positions at $\sim \pm 1'$ away in the direction perpendicular to the slit, and extracted two additional background spectra at positions along the on-source slit. In all of the four different IRS modules, we tried to extract the background spectra at the same position as much as possible, to minimize the flux difference from different modules.

We made an interpolation of a plane in three dimensional space (positions on the IRAC map and wavelength) to obtain a background spectrum at the source position. We estimated an error in each source’s background from the dispersion of four different background spectra, constructed from alternate sets of three out of the four background pointings.

A complete analysis of spectra for all of our 107 YSO candidates will be presented elsewhere (D. An et al. 2009, in preparation). For the current analysis, we selected three targets (Table 1) from among those showing characteristic spectral features of massive YSOs, which include gaseous molecular absorptions from C_2H_2 , HCN, CO_2 (e.g., Lahuis & van Dishoeck 2000; Boonman et al. 2003; Knez et al. 2009), and a solid-phase absorption from CO_2 ice bending mode (e.g., Gerakines et al. 1999).

Both SSTGC 797384 and SSTGC 803187 are associated with a relatively weak radio continuum source (SGR B2(P) and SGR B2(R), respectively; Mehringer et al. 1993). They are on the outskirts of the Sgr B2 molecular cloud (~ 2 pc–4 pc from the well-studied radio source SGR B2(M)), which is one of the most active complexes of compact H II regions in the Galaxy (e.g., Mehringer 1995). Mehringer et al. (1993) derived zero-age main-sequence spectral types of B0 and O6.5 for these compact H II regions, respectively, from the number of ionizing photons. SSTGC 524665 does not have radio continuum emission associated with it. However, it is coincident with an H_2O maser (Forster & Caswell 1989), and is adjacent to a region of $4.5\mu m$ excess emission (Yusef-Zadeh et al. 2009), possibly tracing shocked molecular outflows (e.g., Smith et al. 2006).

For SSTGC 803187, we used a non-standard extraction aperture in SL, because of a nearby source ($\approx 7''$ south of the target) along the slit. We followed the prescription on the IRS data reduction website¹¹ to calibrate the flux. We trimmed the end of the orders to remove the noisy part of spectra, and spectra from different orders in high-resolution modules were averaged using a linear ramp. After background subtraction, the SH and LH spectra were scaled down in flux to LL over the common wavelength interval for SSTGC 797384 and SSTGC 803187. The SL spectra were then scaled to SH. For these sources, we assumed that the flux mismatch is due to narrower slit entrances in SH and SL. For SSTGC 524665, we used the SL as a basis for the scaling, because our observations in LL and LH were contaminated by extended emission from a nearby ($\approx 10''$ southwest of the target) bright source on the $24\mu m$ MIPS image (Carey et al. 2009; Yusef-Zadeh et al. 2009). The background for this target is likely to be over-subtracted, because the target lies on a dark cloud with high extinction, while background spectra were taken at brighter spots. The potential problem of the background subtraction results in H_2 lines (arising from the surrounding sky) appearing in absorption in SSTGC 524665. In the following initial analysis, we did not use LH data for all targets, but focused on the spectral features in other modules.

4. ANALYSIS AND RESULTS

Figure 1 displays background-subtracted spectra of SSTGC 797384, in SL ($\lambda \leq 11.2\mu m$), SH ($11.2\mu m \leq \lambda \leq 19.3\mu m$), and LL ($\lambda \geq 19.3\mu m$). The observed spectrum is characterized by an extremely red SED [$\alpha \equiv d \log(\lambda F_\lambda) / d \log(\lambda) \approx 2$], strong and deep silicate absorptions at $9.7\mu m$ and $18\mu m$, ice absorption features at $6\mu m$, $6.85\mu m$, $13\mu m$, and $15.2\mu m$. Although the presence of forbidden lines indicates that these objects are likely associated with an (ultra-)compact H II region, it could be also due to under-subtracted emissions from the background.

Figure 2 shows gas-phase molecular absorptions at $13.71\mu m$ (C_2H_2 $\nu_5 = 1 - 0$), $14.05\mu m$ (HCN $\nu_2 = 1 - 0$), and $14.97\mu m$ (CO_2 $\nu_2 = 1 - 0$), detected in three YSO candidates. To derive the excitation temperature (T_{ex}) and column density (N_{col}) for each molecular species, we used model spectra from Cami et al. (2006) based on HITRAN04 linelist (Rothman et al. 2005) for C_2H_2 and HCN, and those based on HITEMP (Rothman et al. 1996) for CO_2 . A second order polynomial was used to set a local continuum at $13.30\mu m \leq \lambda \leq 14.55\mu m$ for C_2H_2 and HCN, and $14.77\mu m \leq \lambda \leq 15.06\mu m$ for CO_2 . We did not include isotopes in the computation because of the limited parameter span in the model grids. However, even a relatively high fraction of isotopes in GC ($^{12}C/^{13}C \approx 23$; Wannier 1980) has a negligible impact in the model fitting.

We first made a fit to C_2H_2 , and subtracted its contribution to the absorption near weaker HCN bands. Best-fitting model T_{ex} and N_{col} were found by searching the minimum χ^2 of the fits over $100 K \leq T_{ex} \leq 1000 K$ in steps of $\Delta T_{ex} = 100 K$, and $15 \leq \log N_{col} \leq 18$ for C_2H_2 , $16 \leq \log N_{col} \leq 18$ for HCN, and $16 \leq \log N_{col} \leq 22$ for CO_2 with intervals of 0.1 dex. Solid lines in Figure 2 show our best-fitting models, and their T_{ex} and N_{col} are listed in Table 1. Errors in these parameters were estimated from $\Delta \chi^2$, where 1σ measurement errors were taken from the scatter of flux in the spectra. Systematic

¹¹ See <http://ssc.spitzer.caltech.edu/IRS/calib>.

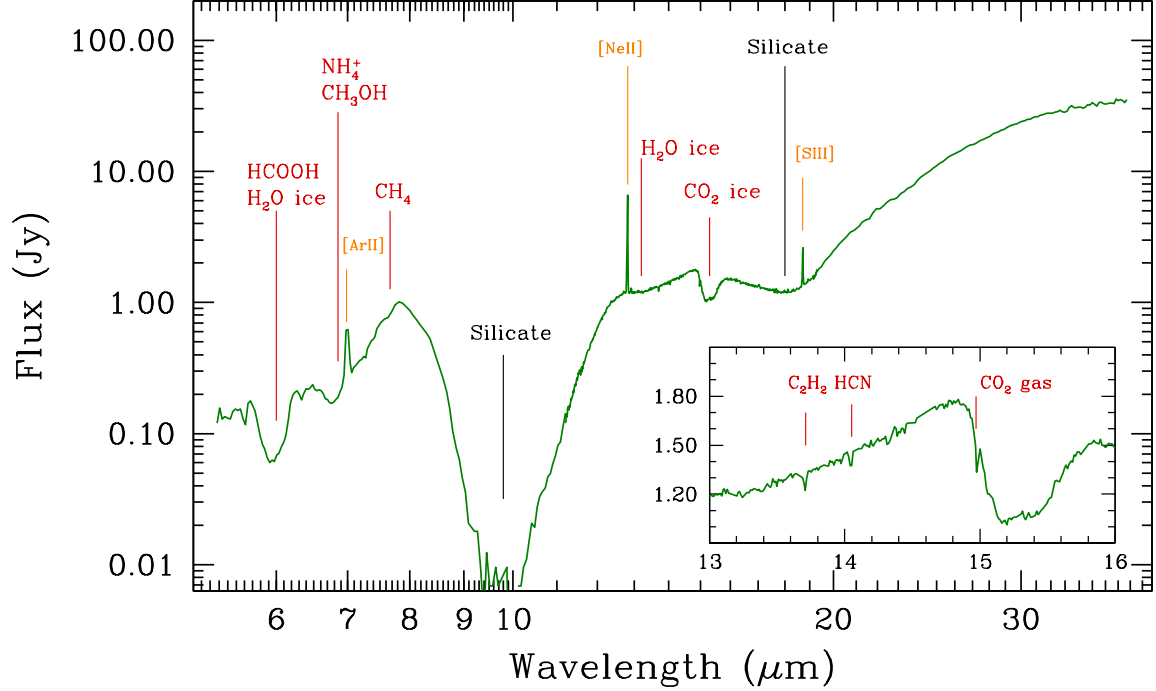


FIG. 1.— Composite IRS spectrum of SSGC 797384. The spectrum is from SL at $\lambda \leq 11.2\mu\text{m}$, SH at $11.2\mu\text{m} \leq \lambda \leq 19.3\mu\text{m}$, and LL at $\lambda \geq 19.3\mu\text{m}$. This composite spectrum is characterized by an extremely red spectral energy distribution, strong and deep silicate absorption, and several molecular gas- and solid-phase absorptions.

TABLE 1
PROPERTIES OF THE SAMPLE

| Quantities | Units | SSTGC 524665 | SSTGC 797384 | SSTGC 803187 |
|--|-------------------------|------------------|------------------|------------------|
| R.A.(J2000.0) | h:m:s | 17:45:39.86 | 17:47:23.68 | 17:47:26.29 |
| Decl.(J2000.0) | d:m:s | -29:23:23.4 | -28:23:34.6 | -28:22:1.5 |
| UKIDSS J^a | mag | ... | 18.23 ± 0.06 | 17.39 ± 0.03 |
| UKIDSS H^a | mag | ... | 14.68 ± 0.01 | 16.60 ± 0.05 |
| UKIDSS K^a | mag | 15.71 ± 0.10 | 12.92 ± 0.01 | 14.37 ± 0.02 |
| IRAC [3.6] ^b | mag | 11.42 ± 0.01 | ... | 12.22 ± 0.02 |
| IRAC [4.5] ^b | mag | 8.63 ± 0.01 | 9.41 ± 0.01 | 8.97 ± 0.01 |
| IRAC [5.8] ^b | mag | 7.08 ± 0.01 | 7.66 ± 0.01 | 7.24 ± 0.01 |
| IRAC [8.0] ^b | mag | 6.13 ± 0.01 | 5.64 ± 0.01 | 5.11 ± 0.01 |
| MIPS [24] ^c | mag | 1.54 ± 0.01 | 0.55 ± 0.01 | ... |
| T_{ex} (C_2H_2 gas) | K | 300 ± 150 | 200 ± 150 | 300 ± 150 |
| T_{ex} (HCN gas) | K | 400 ± 50 | 100 ± 50 | 100 ± 50 |
| T_{ex} (CO_2 gas) | K | 200 ± 50 | 100 ± 50 | 100 ± 50 |
| N_{col} (C_2H_2 gas) | 10^{16}cm^{-2} | 7.9 ± 3.3 | 1.0 ± 0.3 | 2.0 ± 0.8 |
| N_{col} (HCN gas) | 10^{16}cm^{-2} | 15.8 ± 4.6 | 1.0 ± 0.4 | 2.0 ± 0.9 |
| N_{col} (CO_2 gas) | 10^{16}cm^{-2} | 20.0 ± 5.6 | 5.0 ± 1.5 | 7.9 ± 2.8 |
| N_{col} (CO_2 solid) | 10^{19}cm^{-2} | 0.11 ± 0.01 | 0.13 ± 0.01 | 0.21 ± 0.01 |
| N_{col} (H_2O solid, $6\mu\text{m}$) | 10^{19}cm^{-2} | < 1.7 | < 2.3 | < 4.7 |
| N_{col} (H_2O solid, $13\mu\text{m}$) | 10^{19}cm^{-2} | 0.6 ± 0.4 | 1.3 ± 0.4 | 1.9 ± 0.3 |
| N_{col} (H_2) | 10^{22}cm^{-2} | 2.3 ± 0.2 | 5.0 ± 0.5 | 5.8 ± 0.7 |
| $N_{\text{C}_2\text{H}_2}/N_{\text{H}_2}$ | 10^{-7} | 34.3 ± 14.7 | 2.0 ± 0.6 | 3.4 ± 1.4 |
| $N_{\text{HCN}}/N_{\text{H}_2}$ | 10^{-7} | 68.7 ± 20.9 | 2.0 ± 0.8 | 3.4 ± 1.6 |
| $N_{\text{CO}_2,\text{gas}}/N_{\text{H}_2}$ | 10^{-7} | 87.0 ± 25.5 | 10.0 ± 3.2 | 13.6 ± 5.1 |
| $N_{\text{CO}_2,\text{gas}}/N_{\text{CO}_2,\text{solid}}$ | | 0.18 ± 0.05 | 0.04 ± 0.01 | 0.04 ± 0.01 |
| $N_{\text{CO}_2,\text{solid}}/N_{\text{H}_2\text{O},\text{solid}}$ | | 0.18 ± 0.12 | 0.10 ± 0.03 | 0.11 ± 0.02 |
| A_V ($79.7\mu\text{m}$) | mag | 27 ± 3 | 53 ± 5 | 62 ± 7 |
| A_V (color) ^d | mag | 29.0 ± 2.6 | 32.0 ± 2.6 | 27.0 ± 5.4 |

NOTE. — Random errors are shown in the photometry.

^a Aperture3 magnitudes from UKIDSS DR2 (Warren et al. 2007).

^b Photometry from Ramírez et al. (2008).

^c Photometry from MIPS GAL (S. Carey, 2008, private communication).

^d Based on the 2MASS and IRAC color-magnitude diagrams of GC red giant branch stars within $2'$ of the source (Schultheis et al. 2009).

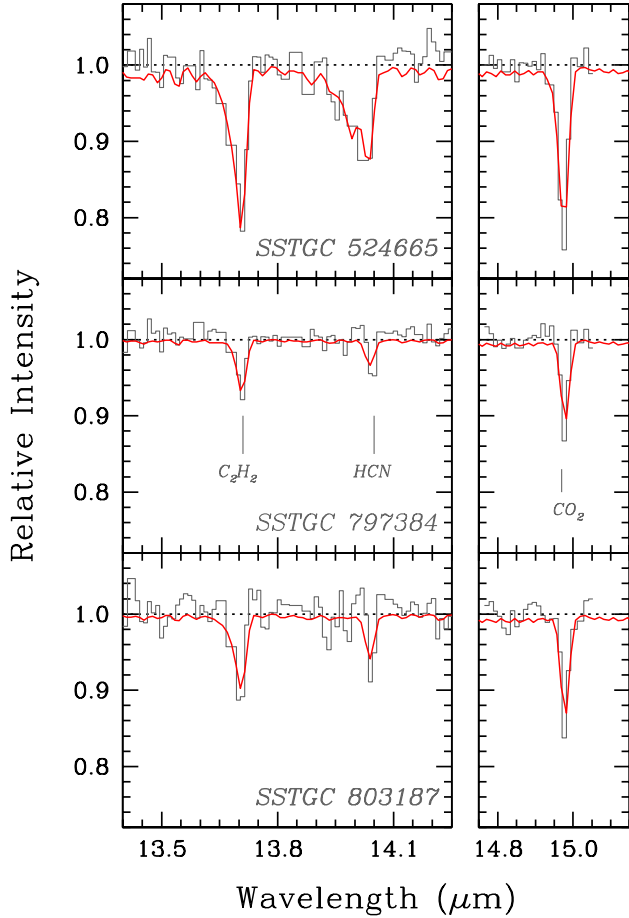


FIG. 2.— Gas-phase molecular absorptions from C_2H_2 $\nu_5 = 1-0$ ($13.71\mu\text{m}$), HCN $\nu_2 = 1-0$ ($14.05\mu\text{m}$), and CO_2 $\nu_2 = 1-0$ ($14.97\mu\text{m}$). Best-fitting models are shown in solid lines.

errors from background subtraction and nodding differences were then added in quadrature. We tested with varying covering factors, but found that best-fitting case yields its value equal to or close to unity.

These gaseous bandheads have been detected in absorption toward YSOs, tracing the warm and dense gas in the circumstellar disk and/or envelopes (e.g., Lahuis & van Dishoeck 2000; Boonman et al. 2003; Knez et al. 2009). They are sometimes detected in the photosphere and/or the circumstellar envelope of carbon-rich asymptotic giant branch stars (e.g. Aoki et al. 1999), but carbon stars have not been found in the GC region (e.g., Guglielmo et al. 1998).

The above estimates are based on models with a Doppler parameter $b = 3 \text{ km s}^{-1}$. The line width measurements of these molecules for several massive YSOs and that of the strongest H_2CO absorption components near SSTGC 803187 are in the range of $b = 1-7 \text{ km s}^{-1}$ (e.g., Mehringer 1995; van der Tak et al. 2000; Knez et al. 2009). There are limited model grids at $b = 10 \text{ km s}^{-1}$ for C_2H_2 and HCN , but T_{ex} and N_{col} were generally found within 2σ from those at $b = 3 \text{ km s}^{-1}$.

Figure 3 shows optical depth spectra of our sources (grey) at $\sim 15.2\mu\text{m}$, where the strong and wide CO_2 ice absorption is seen. We set a local continuum over $14.5\mu\text{m} \leq \lambda \leq 16.5\mu\text{m}$ using a 3rd order polynomial, and followed the prescription in Pontoppidan et al. (2008) to decompose the absorp-

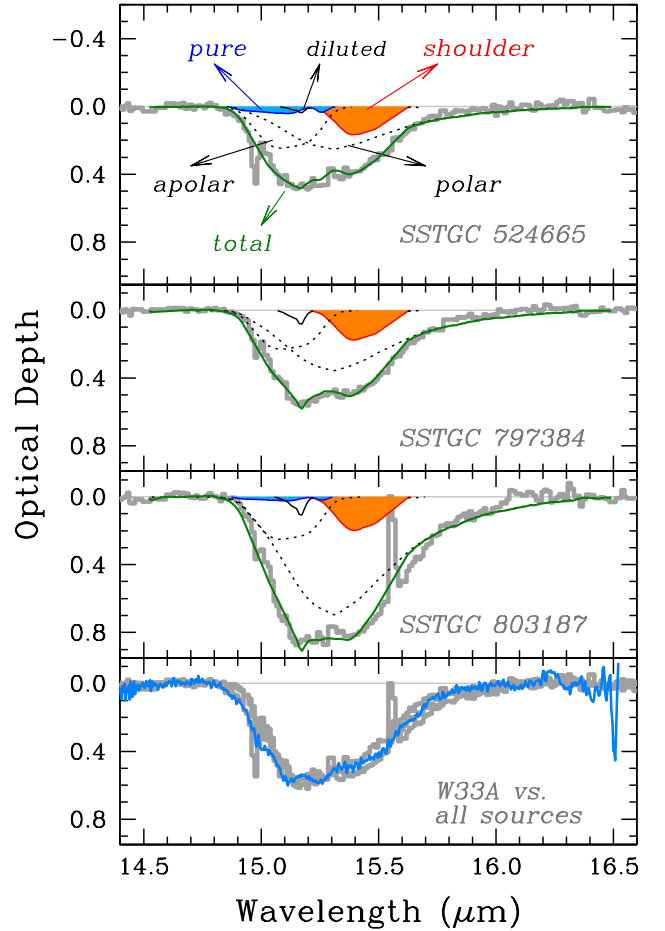


FIG. 3.— Optical depth spectra of solid-phase absorption from the CO_2 ice bending mode. Best-fitting CO_2 ice models and individual CO_2 ice components are shown for each target: polar (dotted line, centered at $\sim 15.3\mu\text{m}$), apolar (dotted line, centered at $\sim 15.1\mu\text{m}$), pure (blue shaded), diluted (black solid line), $15.4\mu\text{m}$ shoulder (orange-shaded), and the sum of these absorption components (green line). The bottom panel shows a comparison of the ice absorption profile between our sources (grey) and massive YSO W33A (blue). The optical depths for our targets were scaled in the bottom panel for comparison.

tion profile with five laboratory spectral components: polar ($CO_2:H_2O = 14 : 100$ at 10 K ; dotted line, centered at $\sim 15.3\mu\text{m}$), apolar ($CO:CO_2 = 100 : 70$ at 10 K ; dotted line, centered at $\sim 15.1\mu\text{m}$), pure CO_2 (15 K ; blue shaded), diluted CO_2 ($CO:CO_2 = 100 : 4$ at 10 K ; black solid line), and $15.4\mu\text{m}$ shoulder CO_2 ice profile (modeled with two Gaussians in wavenumber space; orange shaded). We found a best-fitting set of models from the non-linear least squares fitting routine MPFIT (Markwardt 2009). Green solid line represents the sum of all of the ice components, and the CO_2 ice column density in Table 1 was estimated from the integrated absorption, adopting the integrated line strength $A = 1.1 \times 10^{-17} \text{ cm molecule}^{-1}$ (Gerakines et al. 1995).

Unlike the CO_2 absorption profiles observed in quiescent molecular clouds (e.g. Whittet et al. 2009), the $15.2\mu\text{m}$ band in Figure 3 shows a remarkable double-peaked profile. Double peaked profiles are commonly observed toward YSOs (e.g., Gerakines et al. 1999; Pontoppidan et al. 2008), and are ascribed to pure CO_2 ices resulting from crystallization of heated H_2O -rich ices. However, the double peaks toward the GC candidate YSOs are centered at longer wavelengths

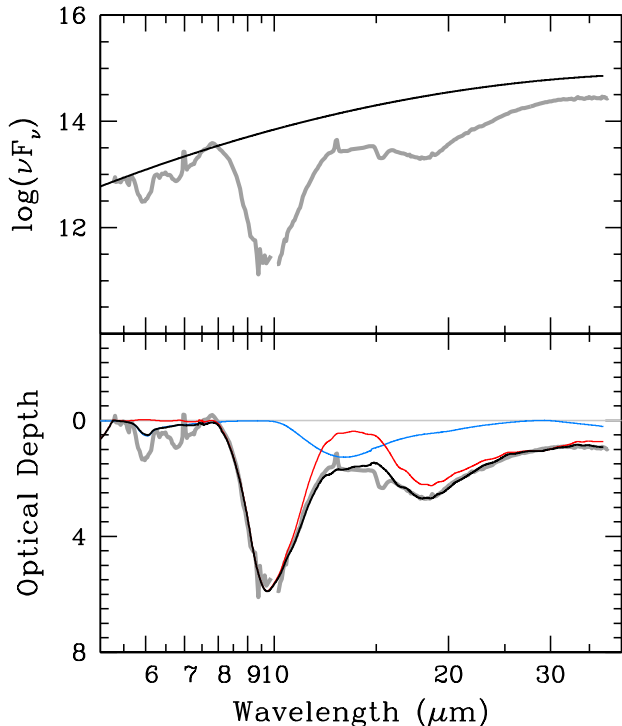


FIG. 4.— Fit to the H₂O ice and silicate absorption for SSTGC 797384. *Top*: SL and LL data (grey), with a best-fitting pseudo-continuum (black line). *Bottom*: Decomposition of optical depth spectra (grey) with the silicate (red) and the laboratory H₂O ice profiles (blue). Black line represents a sum of these two components.

(15.15 μ m and 15.4 μ m vs. 15.10 μ m and 15.25 μ m), and result from CO-rich (15.15 μ m peak) and CH₃OH-rich ices (15.4 μ m peak; see Fig. 3).

The strength of the 15.4 μ m peak is similar to that of the well-studied embedded massive YSO W33A (Gerakines et al. 1999, bottom panel in Fig. 3). It is ascribed to a Lewis acid-base interaction of CO₂ (the Lewis acid) with CH₃OH (Dartois et al. 1999a). Other species could be acting as a base as well, but CH₃OH is preferred due to its high abundance toward W33A: 5%–22% relative to solid H₂O (Dartois et al. 1999b). Two other YSOs (AFGL 7009S, AFGL 2136) show a prominent 15.4 μ m peak, and indeed these sources have high CH₃OH abundances as well (Dartois et al. 1999b; Gibb et al. 2004). This suggests that the GC candidate YSOs have high solid CH₃OH abundances as well.¹² Although the origin of the large quantities of CH₃OH in the previously studied massive YSOs is not fully understood (Dartois et al. 1999a), so far all lines of sight with high solid CH₃OH abundances are associated with star formation, strengthening the idea that the sources studied in this paper are indeed YSOs.

To derive abundances of these molecular absorptions with respect to the hydrogen and solid H₂O column densities, we followed the procedure in Boogert et al. (2008) to fit the H₂O ice and silicate absorption profiles to SL and LL spectra. Figure 4 shows an example for SSTGC 797384. We used the silicate absorption profiles in the line of sight to the GC (GCS 3 spectrum; Kemper et al. 2004) plus a laboratory spectrum of pure amorphous H₂O ice at $T = 10$ K (Hudgins et al. 1993). We simultaneously fit a second-order polynomial for a

pseudo-continuum (i.e., including corrections for the continuous extinction), the silicate profile, and H₂O ice absorption to the $5\mu\text{m} \leq \lambda \leq 32\mu\text{m}$ spectrum. We masked absorption features at 6 μ m, 7 μ m, and 15 μ m, and all unresolved emission lines, before performing a non-linear least squares fit.

Best-fitting parameters are listed in Table 1. We obtained a total hydrogen column density from the optical depth of the 9.7 μ m silicate absorption, assuming $A_V/\tau_{9.7} = 9$ (Roche & Aitken 1985) and $N_{\text{H}}/A_V \approx 1.87 \times 10^{21} \text{ cm}^{-2} \text{ mag}^{-1}$ (Bohlin et al. 1978) at $R_V = 3.1$. The H₂ column density was then approximated by $N_{\text{H}_2} = N_{\text{H}}/2$. The ice column density for the 13 μ m librational H₂O absorption was estimated from the integrated absorption of the best-fitting H₂O model. The H₂O ice column density from the 6 μ m bending mode, fit separately after fixing the continuum and extinction to previously found values, is an upper limit because the 6 μ m absorption is not solely due to H₂O ice. We adopted the integrated line strengths $A = 1.2 \times 10^{-17} \text{ cm molecule}^{-1}$ for the bending mode and $A = 3.1 \times 10^{-17} \text{ cm molecule}^{-1}$ for the librational mode (Gerakines et al. 1995). Errors in these parameters (Table 1) are formal estimates made by varying the range of wavelengths that we used for the 9.7 μ m silicate fitting, or by taking a few different ways of setting the continuum.

The gas-phase molecular abundances relative to H₂ are listed in Table 1. Our derived abundances of $\sim 10^{-7}$ – 10^{-6} for C₂H₂ and HCN are comparable to those found for massive YSOs (Lahuis & van Dishoeck 2000; Knez et al. 2009), although abundances for SSTGC 524665 have large errors. Intervening molecular clouds in the line of sight to the GC are less likely the main cause of these absorptions, because the average HCN abundance of 2.5×10^{-8} (Greaves & Nyman 1996) towards Sgr B2(M) is an order of magnitude lower than our measurements. Our gas-phase CO₂ abundances are an order of magnitude larger than those found towards massive YSOs in Boonman et al. (2003), but our gas to solid abundance ratios for CO₂ are consistent with their estimates (10^{-1} – 10^{-2}). Our abundance of CO₂ ice relative to H₂O ice is within the range (0.10–0.23) found towards massive YSOs (Gerakines et al. 1999).

Finally, Table 1 lists our estimates on A_V from the 9.7 μ m silicate absorption and those from Schultheis et al. (2009), based on the 2MASS and IRAC color-magnitude diagrams of GC red giant branch stars within 2' of the source. Both SSTGC 797384 and SSTGC 803187 have higher A_V values than the average for field stars, implying that a significant fraction of the attenuation is intrinsic to the source. SSTGC 524665 has a lower A_V , comparable to the average value for surrounding field stars. We also note that SSTGC 524665 is located at $b \approx -0.2^\circ$, so it is possible that it is in front of the GC. If we assume a distance of 8 kpc for all three sources, and adopt the extinction of surrounding field stars as the foreground extinction to each source, then we derive stellar masses of $12 \pm 3M_\odot$, $14 \pm 3M_\odot$, $17 \pm 6M_\odot$ for SSTGC 524665, SSTGC 797384, and SSTGC 803187, respectively, by using a grid of YSO models (Robitaille et al. 2006, 2007). More detailed discussion of the model fitting will be presented in a future paper.

To summarize, we presented the evidence from IRS spectra for the first spectroscopic identification of massive YSOs in the GC. In our next paper (D. An, 2009, in preparation), we will present the results for all 107 YSO candidates, together with additional data from millimeter to radio observations, and use them to better understand the nature of these

¹² This needs to be verified by independent L-band spectroscopy of the 3.53 μ m C-H stretch mode of CH₃OH (e.g., Dartois et al. 1999b).

embedded sources.

We thank David Ardila for helpful discussions of the IRS data reduction. We thank Sean Carey for providing us MIPS photometry before publication. D. An and S. Ramírez thank John Stauffer for helpful discussions. This work is based on

observations made with the Spitzer Space Telescope, which is operated by the Jet Propulsion Laboratory, California Institute of Technology under a contract with NASA. Support for this work was provided by NASA through an award issued by JPL/Caltech. This research has made use of the SIMBAD database, operated at CDS, Strasbourg, France.

REFERENCES

- Aoki, W., Tsuji, T., & Ohnaka, K. 1999, *A&A*, 350, 945
 Bohlin, R. C., Savage, B. D., & Drake, J. F. 1978, *ApJ*, 224, 132
 Boogert, A. C. A., et al. 2008, *ApJ*, 678, 985
 Boonman, A. M. S., van Dishoeck, E. F., Lahuis, F., & Doty, S. D. 2003, *A&A*, 399, 1063
 Cami J., Markwick-Kemper A.J., Van Malderen R., 2009, *ApJ* submitted
 Carey, S. J., et al. 2009, *PASP*, 121, 76
 Dartois, E., Demyk, K., d'Hendecourt, L., & Ehrenfreund, P. 1999a, *A&A*, 351, 1066
 Dartois, E., Schutte, W., Geballe, T. R., Demyk, K., Ehrenfreund, P., & D'Hendecourt, L. 1999b, *A&A*, 342, L32
 Fazio, G. G., et al. 2004, *ApJS*, 154, 10
 Felli, M., Testi, L., Schuller, F., & Omont, A. 2002, *A&A*, 392, 971
 Forster, J. R., & Caswell, J. L. 1989, *A&A*, 213, 339
 Gerakines, P. A., Schutte, W. A., Greenberg, J. M., & van Dishoeck, E. F. 1995, *A&A*, 296, 810
 Gerakines, P. A., et al. 1999, *ApJ*, 522, 357
 Gibb, E. L., Whittet, D. C. B., Boogert, A. C. A., & Tielens, A. G. G. M. 2004, *ApJS*, 151, 35
 Greaves, J. S., & Nyman, L.-A. 1996, *A&A*, 305, 950
 Guglielmo, F., Le Bertre, T., & Epchtein, N. 1998, *A&A*, 334, 609
 Houck, J. R., et al. 2004, *ApJS*, 154, 18
 Hudgins, D. M., Sandford, S. A., Allamandola, L. J., & Tielens, A. G. G. M. 1993, *ApJS*, 86, 713
 Kemper, F., Vriend, W. J., & Tielens, A. G. G. M. 2004, *ApJ*, 609, 826
 Knez, C., Lacy, J. H., Evans, N. J., van Dishoeck, E. F., & Richter, M. J. 2009, *ApJ*, 696, 471
 Lahuis, F., & van Dishoeck, E. F. 2000, *A&A*, 355, 699
 Markwardt, C. B. 2009, arXiv:0902.2850
 Mehringer, D. M. 1995, *ApJ*, 454, 782
 Mehringer, D. M., Palmer, P., Goss, W. M., & Yusef-Zadeh, F. 1993, *ApJ*, 412, 684
 Morris, M., & Serabyn, E. 1996, *ARA&A*, 34, 645
 Omont, A., et al. 2003, *A&A*, 403, 975
 Pontoppidan, K. M., et al. 2008, *ApJ*, 678, 1005
 Ramírez, S. V., Arendt, R. G., Sellgren, K., Stolovy, S. R., Cotera, A., Smith, H. A., & Yusef-Zadeh, F. 2008, *ApJS*, 175, 147
 Robitaille, T. P., Whitney, B. A., Indebetouw, R., Wood, K., & Denzmore, P. 2006, *ApJS*, 167, 256
 Robitaille, T. P., Whitney, B. A., Indebetouw, R., & Wood, K. 2007, *ApJS*, 169, 328
 Roche, P. F., & Aitken, D. K. 1985, *MNRAS*, 215, 425
 Rothman, L. S., et al. 1996, *Journal of Quantitative Spectroscopy and Radiative Transfer*, 60, 665
 Rothman, L. S., et al. 2005, *Journal of Quantitative Spectroscopy and Radiative Transfer*, 96, 139
 Schuller, F., Omont, A., Glass, I. S., Schultheis, M., Egan, M. P., & Price, S. D. 2006, *A&A*, 453, 535
 Schultheis, M., Lançon, A., Omont, A., Schuller, F., & Ojha, D. K. 2003, *A&A*, 405, 531
 Schultheis, M., Sellgren, K., Ramírez, S., Stolovy, S., Ganesh, S., Glass, I. S., & Girardi, L. 2009, *A&A*, 495, 157
 Skrutskie, M. F., et al. 2006, *AJ*, 131, 1163
 Smith, H. A., Hora, J. L., Marengo, M., & Pipher, J. L. 2006, *ApJ*, 645, 1264
 Stolovy, S., et al. 2006, *Journal of Physics Conference Series*, 54, 176
 van der Tak, F. F. S., van Dishoeck, E. F., Evans, N. J., II, & Blake, G. A. 2000, *ApJ*, 537, 283
 Wannier, P. G. 1980, *ARA&A*, 18, 399
 Warren, S. J., et al. 2007, arXiv:astro-ph/0703037
 Werner, M. W., et al. 2004, *ApJS*, 154, 1
 Whittet, D. C. B., Cook, A. M., Chiar, J. E., Pendleton, Y. J., Shenoy, S. S., & Gerakines, P. A. 2009, *ApJ*, 695, 94
 Whitney, B. A., Wood, K., Bjorkman, J. E., & Cohen, M. 2003, *ApJ*, 598, 1079
 Whitney, B. A., Indebetouw, R., Bjorkman, J. E., & Wood, K. 2004, *ApJ*, 617, 1177
 Yusef-Zadeh, F., et al. 2009, arXiv:0905.2161